

A topological classifier to characterize brain states: When shape matters more than variance

Aina Ferrà¹, Gloria Cecchini¹, Fritz-Pere Nobbe Fisas¹,
Carles Casacuberta^{1,2}, Ignasi Cos^{1,2,3}

Abstract

Despite the remarkable accuracies attained by machine learning classifiers to separate complex datasets in a supervised fashion, most of their operation falls short to provide an informed intuition about the structure of data, and, what is more important, about the phenomena being characterized by the given datasets. By contrast, topological data analysis (TDA) is devoted to study the shape of data clouds by means of persistence descriptors and provides a quantitative characterization of specific topological features of the dataset under scrutiny.

In this article we introduce a novel TDA-based classifier that works on the principle of assessing quantifiable changes on topological metrics caused by the addition of new input to a subset of data. We used this classifier with a high-dimensional electro-encephalographic (EEG) dataset recorded from eleven participants during a decision-making experiment in which three motivational states were induced through a manipulation of social pressure. After processing a band-pass filtered version of EEG signals, we calculated silhouettes from persistence diagrams associated with each motivated state, and classified unlabeled signals according to their impact on each reference silhouette. Our results show that in addition to providing accuracies within the range of those of a nearest neighbour classifier, the TDA classifier provides formal intuition of the structure of the dataset as well as an estimate of its intrinsic dimension. Towards this end, we incorporated dimensionality reduction methods to our procedure and found that the accuracy of our TDA classifier is generally not sensitive to explained variance but rather to shape, contrary to what happens with most machine learning classifiers.

Introduction

The ability to capture detailed high-dimensional statistics of large datasets has earned deep learning the reputation of general solver for a wide range of complex problems [1, 2, 3]; from image analysis [4, 5] to object recognition [6], climate prediction [7, 8], genomic analyses and behavioural prediction [9] or hidden variable identification for brain dynamics [3]. However, the downside of deep learning, as of any black-box AI technique, is the poor explainability of results and of the structure of the datasets, which necessarily bounds interpretability [10, 11, 12]. Possibly more puzzling, deep learning commits rare but unpredictable clustering errors, such as confusing a lion with a library, or a lamp with a traffic light [13]. While odd, it is precisely the lack of a principled explanation leading to these unpredictable failures that makes of deep learning a technique with significant trust issues, in particular for AI in life-threatening decision-making scenarios.

¹Departament de Matemàtiques i Informàtica, Universitat de Barcelona (UB), Gran Via de les Corts Catalanes, 585, 08007 Barcelona, Catalonia, Spain

²Institut de Matemàtica de la Universitat de Barcelona (IMUB)

³Serra-Hunter Fellow Programme, Catalonia, Spain

This work was supported by the CERCA Programme of the Catalan Government (I. Cos); by the European Union's Horizon 2020 Framework Programme for Research and Innovation under the Specific Grant Agreements No 945539, Human Brain Project SGA3 (I. Cos), and by MCIN/AEI/10.13039/501100011033 under grant PRE2020- 094372 (A. Ferrà) and projects PID2019-105093GB-I00 (I. Cos, A. Ferrà) and PID2020-117971GB-C22 (C. Casacuberta).

Keywords: Topological data analysis; machine learning; classification; neuroscience; brain states; explainability

Mathematics Subject Classification: 55N31, 92C20, 62R40, 68T09

By contrast, topology is a branch of mathematics devoted to characterize the structure of high-dimensional datasets by formal means [14, 15]. In brief, if a dataset can be represented as a point cloud in a hyperspace, topological data analysis (TDA) may characterize its connectivity, cycles within the cloud, or the number of clusters it contains, by means of a set of metrics (or summaries) that encompass all dimensions. Therefore, although not conceived for problem solving or to capture data variability per se, if we apply TDA to datasets of different classes within a classification problem, it will yield summaries specific to each class. Consistent with this, some studies have proposed the use of TDA metrics as a preliminary stage to extract features for machine learning classifiers, e.g., for medical image analysis [16, 17, 18], chemical components [19, 20], or computer science problems [21]. Thus, these classification problems do not operate in the multidimensional dataset or in a subsequent reduced dimensionality space [22, 23], but rather in the domain of meaningful topological feature vectors [24, 25, 26], with a consequent interpretability gain.

While this is a promising research avenue that facilitates tracing class specificities back to the structure of data, our predicament is to use TDA as a classifier. In brief, if different subsets of data (belonging to different classes) yield different topological summaries, it is plausible that the differences across summaries themselves can be directly exploited for classification purposes. Towards this end, here we introduce a classifier inspired on this principle. The bonus of such a classifier with respect to a classical machine learning one is that, in addition to an accuracy and a confusion matrix, it should provide an informed intuition of the specific aspects of the dataset responsible for separability of classes. Other approaches for classification or semi-supervised learning using topological persistence have been undertaken in [27] and [28].

As a testbed for our classifier, we used a challenging classification problem in dire need of explainability, which is the state cortical brain network during performance of specific tasks [29, 30, 31]. In particular, we focused on the characterization of the brain network of motivation, as defined in the context of a decision-making task between precision reaches [32] by different levels of social pressure. We analysed a set of electro-encephalograms (EEG) recorded as the decisions unfolded from eleven participants, by turning the problem into a three-class classification problem, in which we aimed at explaining the differences across these states on the grounds of our TDA classifier. We yield two main results: first, the TDA classifier obtained accuracies comparable to those obtained by a nearest neighbour classifier; second, accuracy strongly depended on the shape of the data but not on the amount of explained variance achieved by a dimension-reducing projection. In summary, specific topological descriptors indeed provide reliable ensemble characterizations of high-dimension neural states, and yields an avenue for data explainability complementary to machine learning.

1 Materials and methods

1.1 Persistence summaries

Topological data analysis is a branch of mathematics based on algebraic topology aiming to detect and represent structural features of datasets, such as sparseness, flares or cycles. Its main tool is persistent homology [33, 34, 35, 36], an algebraic characteristic of simplicial complexes equipped with a real-valued filtering function. Persistent homology is well suited for describing the shape of a point cloud along a range of resolution scales.

Formally, a point cloud is a finite subset $X \subset \mathbb{R}^d$ for some $d \geq 2$ viewed as a metric space by means of the Euclidean distance. The *Vietoris–Rips filtration* [37, 38] associated with X is a nested family of abstract simplicial complexes $V_t(X)$ for $t \geq 0$, where $V_t(X)$ has a vertex for each point in X and a k -simplex with $k \geq 1$ for each collection of points v_0, \dots, v_k in X such that $\|v_i - v_j\| \leq 2t$ for all i, j .

The inclusions $V_s(X) \subseteq V_t(X)$ for $s \leq t$ induce morphisms $H_n(V_s(X)) \rightarrow H_n(V_t(X))$ for $n \geq 0$, where H_n denotes n -dimensional simplicial homology [39]. We compute homology with coefficients in a finite field—we use the GUDHI Python Library [40] with a default choice of the field \mathbb{F}_{11} . The *birth parameter* b of a homology generator in dimension n is the smallest value of t such that $H_n(V_t(X))$ contains the given generator, and the *death parameter* d is the smallest value of t where that generator is mapped to zero. The *persistence* or *lifetime* of a homology generator is the difference $d - b$.

The *persistence diagram* associated with the Vietoris–Rips filtration of X in homological dimension n consists of all birth-death pairs (b, d) for a basis of n -dimensional homology generators, drawn above the diagonal $y = x$ of the first quadrant in \mathbb{R}^2 . Points that are close to the diagonal (i.e., with a short lifetime) may correspond to inessential phenomena, while those with large lifetimes reflect persistent shape features of the given dataset. In some cases, however, the distribution of points near the diagonal carries relevant information that should not be neglected.

Persistence diagrams in dimension 0 contain information about connected components of Vietoris–Rips complexes, specifically about the way in which connected components merge as the parameter t increases. Persistence diagrams in dimension 1 depict the appearance and disappearance of 1-cycles, while persistence diagrams in dimensions $n \geq 2$ represent the evolution of n -dimensional cavities in the Vietoris–Rips complexes.

Two fundamental results endow persistent homology with the robustness required for a rigorous mathematical theory with real-world applications. The first one is the fact that persistence diagrams are well-defined [34], that is, do not depend on the choice of a basis of homology generators. The second one is *stability* [41, 42], i.e., small perturbations in the data can only yield minor perturbations in the corresponding persistence diagrams.

Dissimilarity between persistence diagrams can be measured by the *bottleneck distance*, to which the stability theorem refers when claiming that two diagrams are close to each other. The bottleneck distance between two diagrams D_1 and D_2 is defined as the largest coordinate-wise distance between points $x \in D_1$ and $\varphi(x) \in D_2$, where φ is the matching that minimizes the outcome among all possible bijections between D_1 and D_2 , admitting points in the respective diagonals as eligible matches [33]. However, persistence diagrams equipped with the bottleneck distance are not well-suited for statistical analyses. On one hand, it is not feasible to compute averages of persistence diagrams [43]; on the other hand, it is necessary for many purposes to work with representations of persistence diagrams in Hilbert spaces. For this, a convenient summary of a persistence diagram is its *landscape* [44, 45]. A persistence landscape is a sequence of piecewise linear functions obtained by rotating the diagram 45 degrees clockwise (Fig. 1) and choosing the k -highest point for each $k \geq 1$ in the resulting figure [44].

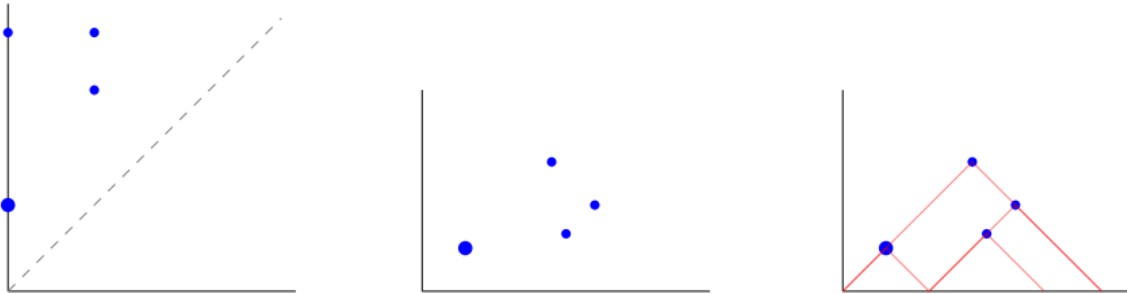


Figure 1: Persistence landscape (right) obtained from a persistence diagram (left) by means of a 45° rotation and rescaling (middle). Dots of larger size indicate multiplicity.

More precisely, for each point (b, d) in a given persistence diagram, one considers a *tent function* $\Lambda_{(b,d)}(t) = \max\{0, \min\{t-b, d-t\}\}$ and defines $\lambda_k: \mathbb{R} \rightarrow \mathbb{R}$ for each $k \geq 1$ as $\lambda_k(t) = \text{kmax}\{\Lambda_{(b_i,d_i)}(t)\}$, where $\{(b_i, d_i)\}$ is the set of all points in the given persistence diagram and kmax returns the k -th largest value of a given set of numbers, or zero if there is no k -th largest value. Consequently, $\lambda_k = 0$ for sufficiently large values of k . The first landscape levels $\lambda_1, \lambda_2, \dots$ represent the most significant features from the persistence diagram, while the last ones correspond to points near the diagonal and hence ephemeral phenomena.

Despite their usefulness, persistence landscapes are memory-wise expensive when handling large datasets. To overcome this problem, *silhouettes* were introduced in [46] by considering a weighted average of the tent functions used to build a landscape:

$$\phi_w(t) = \frac{\sum_{i=1}^m w_i \Lambda_{(b_i,d_i)}(t)}{\sum_{i=1}^m w_i}.$$

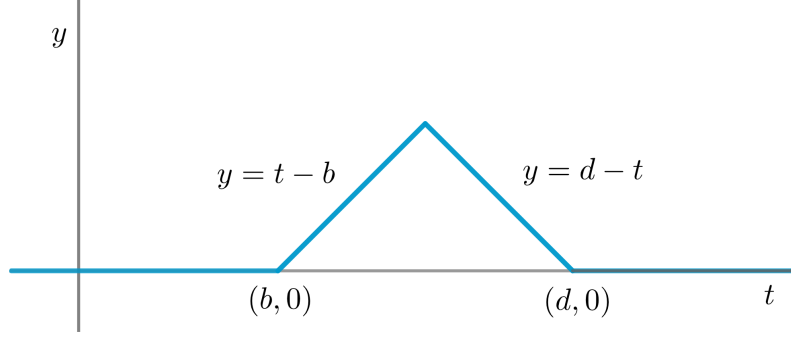


Figure 2: Tent function for a birth parameter b and a death parameter d .

In this article we choose lifetimes $w_i = d_i - b_i$ as weights and use the resulting silhouettes as persistence summaries for our analyses. Since lifetimes need to be finite, we discard points with infinite persistence in dimension zero.

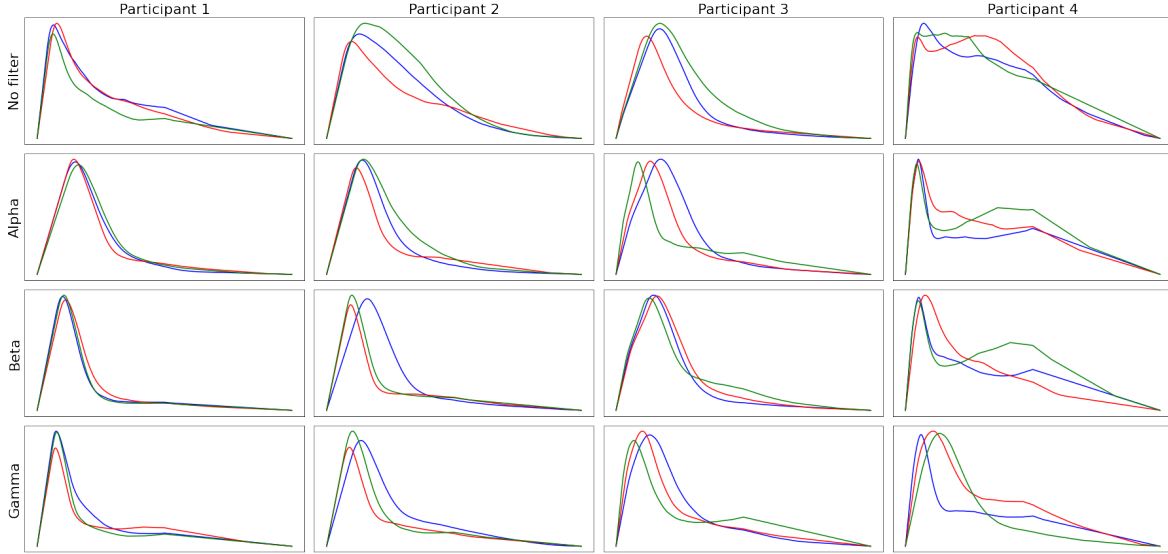


Figure 3: Silhouettes from persistence diagrams in dimension zero for each motivational state (M_0 : blue, M_1 : red, M_2 : green) for each frequency band (alpha, beta, gamma) plus the unfiltered dataset (no filter) for participants 1-4 in the space of sources without dimensionality reduction. The datasets are described in the next subsections.

We measure dissimilarity between persistence diagrams by discretizing silhouettes into vectors of 1000 components and computing Euclidean distances between such vectors.

Only persistence silhouettes corresponding to homological dimension zero were used for classification purposes. Higher dimensions were not considered in the study since generically no significant variation of persistence summaries can be expected by adding a single point to a training dataset, except in dimension zero.

1.2 A topological classifier

A typical classification process starts with partitioning a labelled dataset D into training and testing sets, assuming knowledge of the label class c to which each input x belongs in the training set.

Accuracy is defined as the percentage of correctly classified datapoints from the testing set.

Thus, if we have a dataset D containing m training datapoints as given by $D = \{(x_i, c_i)\}$ with $i = 1, \dots, m$, the purpose of classifying is, for any given point x , to return its best predicted class $c(x)$. Therefore, a critical question for a classifier algorithm is to define an appropriate metric of similarity between datapoints, so that similar points belong the same class. Typically, given two points x and y , similarity is quantified by a distance function $d(x, y)$ between them. For example, the *nearest neighbour algorithm* uses the Euclidean distance. Given a datapoint x from the testing dataset, and given the training data $\{(x_i, c_i)\}$, the nearest neighbour algorithm classifies x as follows:

1. Calculate the Euclidean distance $d_i = d(x, x_i)$ of the point x to each of the training points x_i .
2. Find a point x_{i_*} in the training dataset such that $d_{i_*} = \min_i \{d_i\}$.
3. Assign the class label $c(x) = c_{i_*}$. If there are equidistant points with different labels, the algorithm selects the class containing the largest number of points.

Our persistence-based topological classifier follows instead the next procedure:

1. The training set is split into classes according to given labels.
2. For each class label c in the training set, calculate the corresponding silhouette S_c in homological dimension 0 with lifetimes as weights.
3. To classify an input x from the testing set, add x to the cloud of training datapoints X_c of each class label c . Then, recompute the persistence silhouettes $S_{c,x}$ for the datasets $X_c \cup \{x\}$, and finally calculate the Euclidean distance $d(S_c, S_{c,x})$ between the newly obtained silhouettes and the former ones.
4. Assign the class label $c(x) = c_*$ where $c_* = \operatorname{argmin}_c \{d(S_c, S_{c,x})\}$.

The underlying assumption is that point clouds from different classes exhibit recognizably different shapes. More precisely, if we add a point to the point cloud of the correct class, the resulting topology should not fundamentally change, meaning that all distances should remain small. By contrast, if a point is added to a point cloud of a different class, then the topology should be altered more visibly.

1.3 Time series of brain states of motivation

For practical purposes, we opted for testing our TDA classifier on a dataset previously recorded, rather than opting for recording a new one ad-hoc to this end. The dataset and the context of its recording is described next. In addition to having an advantageous set of baseline results to fall back on for comparison purposes, which would undoubtedly facilitate the validation of the TDA classifier, we specifically chose this dataset to task the TDA classifier to provide a richer characterization of the dataset underlying structure than machine learning algorithms, and of the processes generating that dataset.

Reward and motivation are two fundamental drives of human behaviour. Consistent with this, a large number of studies in neuroscience have intended a careful identification and characterization of the brain centers of reward processing, most often based on analyses of functional magnetic resonance imaging (fMRI) recordings in humans. However, one of the questions that remains to be fully answered is how the different expressions of motivation are distributed across the brain network. In other words, what is the distribution of the brain network of social motivation?

To answer this question, we refer to a study carried out with eleven participants in Barcelona [32], in which high-density electro-encephalograms (EEG) were recorded from human participants during a decision-making task in which motivation was modulated via social pressure. The goals of this task were the formal characterization of the influence of social pressure on movement decisions and on choices of movement parameters to make precision reaches and of the brain network of social motivation [32]. The *manipulation of motivation* was performed by means of social pressure, as a function of the participant’s aiming accuracy with respect to that of a virtual partner. In brief, the

idea was that the presence of the partner would introduce an implicit bias to boost the participant to improve their accuracy. We informed the participant that they would perform within a community of players, and that at each block, they would have a different partner from this community to perform alongside. To reinforce the belief on the existence of a partner, at the end of each trial we showed a horizontal green bar displaying the accuracy attained, normalized between 0 and 100%, over a red bar displaying the partner’s accuracy. The purpose of the simulated partner was to introduce an implicit bias to modulate the participant’s motivation to reach more accurately. Thus, we instructed each participant not to compete to just focus on their own performance, and to disregarding the partner. To parameterize the bias introduced by the presence of the virtual partner, we used partners of two types, less or more accurate than the participant (Fig. 1D). We also matched the gender of partner to that of the participant to control for cross-gender effects.

The level of social pressure remained constant throughout each block, maintaining the same virtual partner. The partner was varied across each block in a counter-balanced fashion. Each participant performed two sessions of six blocks each, with each block consisting of one-hundred and eight trials. The six blocks were distributed into two groups of three. Each group consisted of one block solo and two blocks each alongside a partner of a lesser/higher aiming skill. The goal of this manipulation was to induce three distinct motivated states as a function of the level of social pressure exerted:

- Solo, the participant performed alone. No social pressure in this condition.
- Easy, the participant performed alongside a virtual partner of a lesser skill than them. Some social pressure was expected in this condition.
- Hard, the participant performed alongside a virtual partner of a higher skill than them. High pressure was expected in this condition.

The dataset used for TDA analysis recorded during performance of this task. The *structure of the dataset* consisted of EEG fragments from each of the participant’s recordings, for each level of induced social pressure. Since we were specifically interested in assessing the changes on the motivation baseline, we selected an interval of interest of 1200 ms at each trial, starting 800 ms before the first stimulus onset —the initial cue, and ending 400 ms later (see Fig. 4A)— before any movement or stimuli were presented on the screen at that trial. Each channel was filtered with a 4th order notch filter at 50, 100 and 150 Hz to remove electrical interference caused by the power supply line, and a 4th order bandpass Butterworth filter between 0.1 and 100 Hz to constrain the band of interest. Electrodes with EEG level exceeding either 200 V or voltage step/sampling 50 V within intervals of 200 ms were removed from further analysis. Baseline was corrected, and the datasets were z-scored by using the recordings during trial block types 1 and 2 of each session —when the participant was playing solo, as a reference for baseline motivation. Eye related artefacts were removed by means of independent component analysis (ICA), implemented in with custom-made Field-trip open-source toolbox (www.fieldtrip.com) and EEGLAB scripts (<http://scn.ucsd.edu/eeglab>, UC San Diego, CA, USA). The procedure to identify eye-movement related sources was semi-automatized, first correlating each source obtained with the signal from the electrodes recording eye movements to obtain a first metric of relatedness. Second, we visually inspected all sources to corroborate that their shape and spatial location matched those of ocular artefacts. Eye-related sources were removed and the cleaned signal obtained by inverting the ICA process. A final source space was obtained by applying ICA again, but forcing the resulting space to be of smaller dimension than the dimension of the electrode space, in order to capture a few independent areas of the brain whose signals are sent to the electrodes. Thus the dimension of the source space may be different for each participant —usually less than 50.

The computation of the projection of the data on the source space was performed with custom-made MATLAB scripts based on the EEGLAB library, combined with the electrode spatial location map. The Brain Products Unicap 64 (Brain Products GmbH, Gilching, Germany) configuration was used to establish a spatial reference between the electrode placement and to perform source localization. We assumed a spherical head model. Please, note that ICA projections serve a dual purpose: first, to distribute the information contained in the electrode signals along directions of maximal inter-independence between dimensions. Second, to provide a rough anatomical estimate for the location of the brain sources generating the signals recorded by the electrodes, on the brain cortical surface.

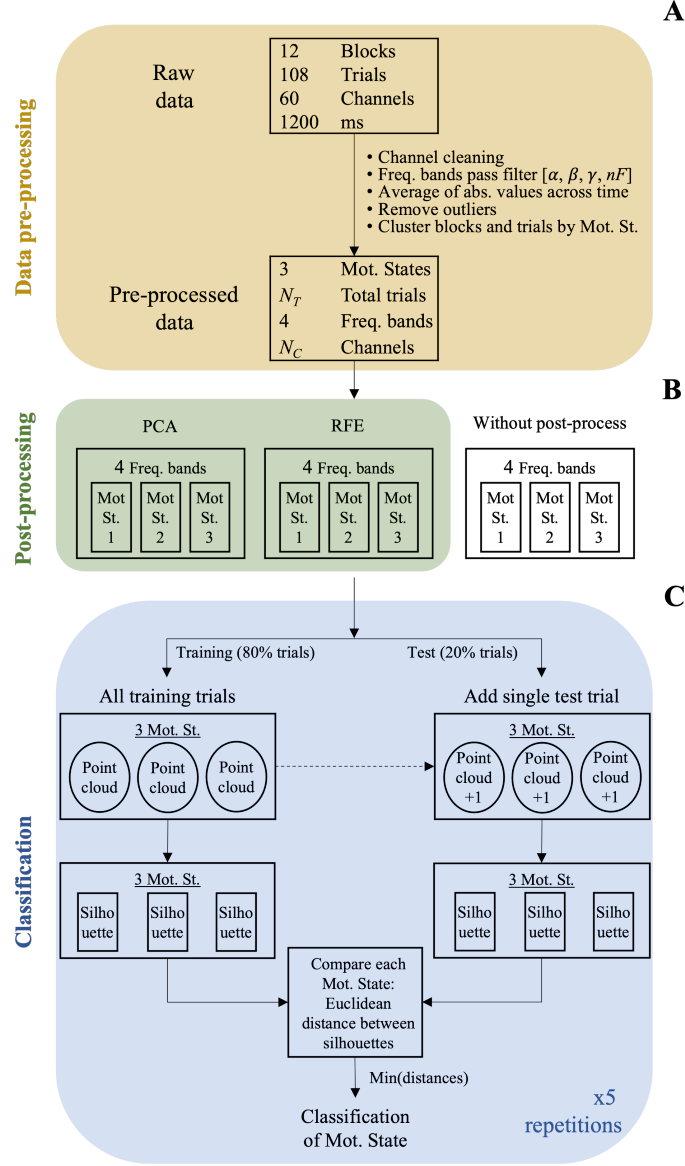


Figure 4: **A. Pre-processing schematic.** Channels are either electrodes or sources. Each channel of raw data is band-passed filtered into the three typical EEG bands (α : low; β : medium; γ : high). Channels containing artifacts or noisy information are removed, resulting in a final number of N_C channels. Absolute values of time series are averaged for each channel. Outliers are removed from the resulting dataset. **B. Post-processing schematic.** Principal component analysis (PCA) or recursive feature elimination (RFE) are used. No post-processing is performed on raw data. **C. Classification schematic.** 80% of the data is used for training purposes and 20% for testing ones. Persistence silhouettes are used for classification.

In summary, the dataset consists, per trial, of a variable number of channels (electrodes or sources), denoted as N_C , lasting 1200 ms each. Each participant performed 12 blocks of 108 trials. Note that 12 blocks were recorded during two different sessions, containing 6 blocks each, balancing out the number of motivated blocks.

1.4 Analysis pipeline

For each of the eleven participants in the study (four male and seven female aged 55 ± 5.8) the dataset consisted of $1200 \text{ ms} \times 60$ electrodes EEG segments, repeated over 12 blocks (six per session) of 108 trials each (Fig. 4A). The level of social pressure leading to a specific motivated state was maintained constant across each block, and there were four blocks for each motivated state (two each session).

Pre-processing

- First, data were visually inspected to identify and remove noisy or artefactual channels from further analysis. We call N_C the number of channels surviving this process.
- Second, EEG signals encompass a spectrum ranging 0.01–100 Hz, which we distributed into the three typical frequency bands: α (8–15 Hz), β (15–32 Hz), γ (32–80 Hz), obtaining three band-passed versions of the original temporal series. Each of these signals were analyzed in the same fashion, and independently of each other, alongside with an unfiltered baseline version of the original signal. This distribution of frequency bands responds to the established association of brain function with power fluctuations in specific bands and electrode locations. Band-pass filtering was performed with custom-made scripts in Python, using the `iirfilter()` function from the `scipy.signal` library [47]. Previous analyses on previous studies suggest that motivation related modulations belong in the high-gamma band, thus suggesting that motivation related biases should be better encoded in the higher frequency band [32].
- Third, we averaged each electrode or source absolute value across the 1200 ms window of observation, obtaining a dataset organised as a matrix of N_T trials by N_C channels. Outliers exceeding twice the standard deviation from the average of norms of datapoints were disregarded from further analysis.

Our classification was conducted within the signals obtained for each band-pass independently, as well as with an unfiltered version of the original signal.

Post-processing

Two different dimensionality reduction methods were used to the pre-processed dataset by means of the `sklearn` library [48], yielding dimensions between 2 and 10.

- Principal component analysis (PCA) is a linear projection onto a lower-dimensional space of principal components, where the first principal component of a point cloud is the one that explains the most variance, and each successive principal component explains the most variance in what is left once the effect of the previous components is removed [22].
- Recursive feature elimination (RFE) consists of successively removing coordinates with the lowest impact on the accuracy of a classifier [49]. In our study, RFE was applied to the pre-processed dataset using a logistic regression model to assign weights to the features.

Classification

Once each dataset (for each frequency band) was properly formatted, it was input into the TDA classifier (Fig. 4B). From this point on, trials were considered as points of a cloud to be classified. The classification operation was carried out as described in the topological classifier subsection. Each classification was repeated 5 times and the resulting accuracies averaged over the 5 repetitions. At each repetition, post-processed datasets were partitioned into 80% training data and 20% testing data. In the case of raw data (no dimensionality reduction), pre-processed datasets were used.

The analyses were performed both with the original signals in electrode space, as well as with those projected onto the brain source space.

2 Results

To first establish a baseline of accuracy that would enable an assessment of the influence of dimensionality reduction techniques on the classification process, we tested our TDA classifier on the original EEG signals projected on source space; see Analysis pipeline. Second, we tested the influence of two dimensionality reduction methods (PCA and RFE) on the classification process. Third, to further assess the influence of the ICA projection on the classifier, we also tested the original dataset, as collected in electrode space. Each of the aforementioned tests were performed with each of the band-passed version of the EEG signals (α , β , γ), independently; see Analysis pipeline.

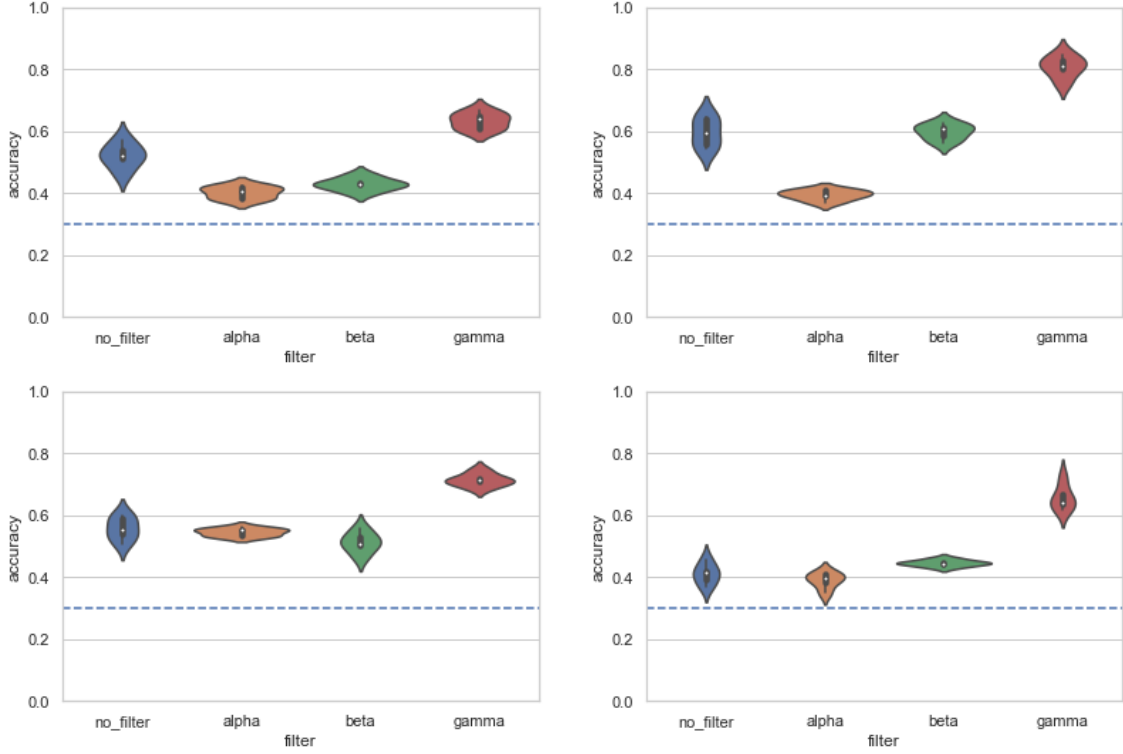


Figure 5: Accuracies of the topological classifier on source space by frequency band using the space of sources and without dimensionality reduction for participants 1, 3 (top right), 7 and 11. A complete set of results for all participants is given in the Appendix.

Classification on source space

We performed the classification for the dataset of each participant within each frequency band, using the data projected onto source space prior to any dimensionality reduction. Fig. 5 shows the classification accuracies obtained by the TDA classifier for four typical participants. Although the classification yielded some differences across participants, the main result obtained is a consistent top accuracy in the gamma band for all participants but one, ranging in average between 60% to 80%. Violin plots in Fig. 5 encode median, interquartile range, and a kernel-smoothed probability density of the data. The violin plots were performed using the `seaborn` library [50].

Using this as a baseline, we assessed the influence of dimensionality reduction on the classification. The underlying hypothesis is that, if the TDA classifier focuses on elements of the shape of the point cloud to determine separability, datasets rearranged in specific spaces should yield point clouds with shapes more favourable to be classified. To test this, we performed two complementary dimensionality reduction techniques. For each participant dataset, we first performed a principal component analysis

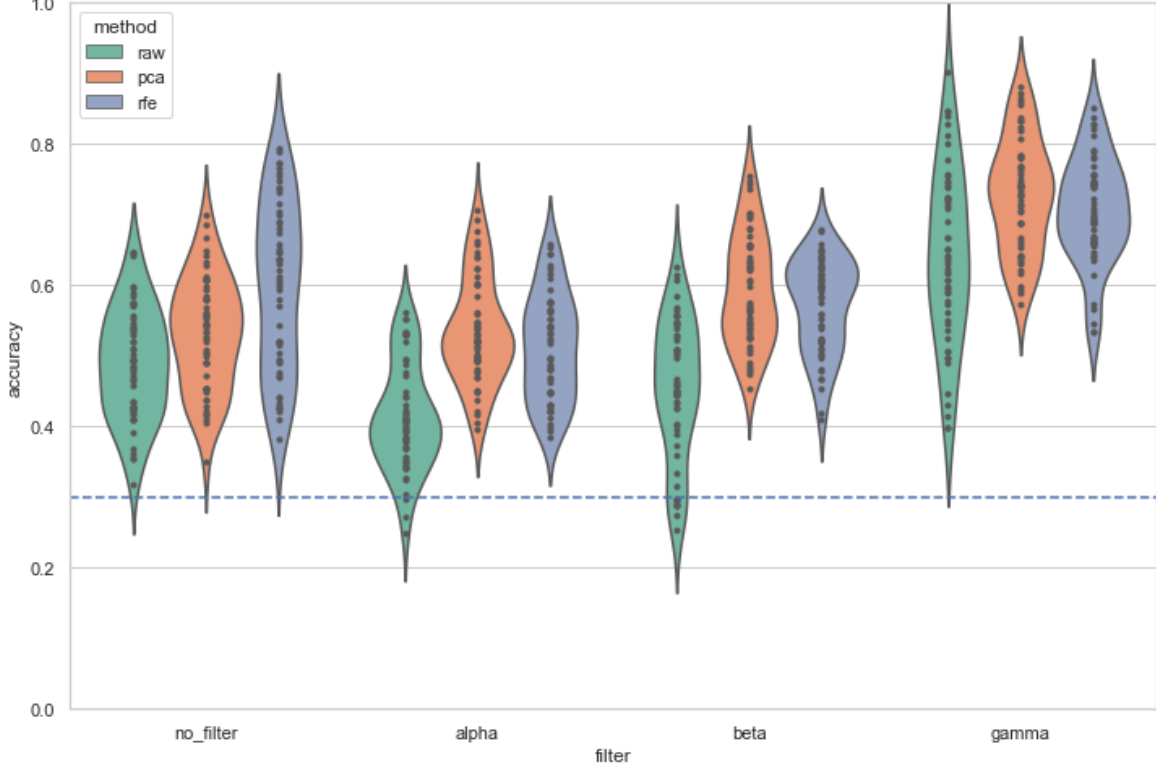


Figure 6: Comparison of baseline accuracies (*raw*) of the topological classifier on source space for each frequency band with accuracies obtained after dimensionality reduction with principal component analysis (*pca*) and recursive feature elimination (*rfe*), for participants 1 to 11. Each violin contains accuracy percentages of five repetitions for each participant.

(PCA) decomposition, selecting the dimensions that would explain until 95% of data variance for all participants, ultimately retaining from 2 to 10.

In a complementary fashion, we performed a second dimensionality reduction technique on the same datasets. Unlike PCA, recursive feature elimination (RFE) is based on assessing the contribution of specific components of the original dataset to the classification process. When performed in source space, this results in a ranking of sources. The datasets resulting from PCA and RFE were also classified for each participant and for each frequency band. The summary results obtained from these classifications are listed in Fig. 13, showing the accuracies of the topological classifier for each of the eleven participants, for each frequency band and for each dimensionality reduction method. The accuracies in Fig. 13 have been obtained by averaging the accuracies obtained from five repetitions for each dimension. Since there are three distinct classes, chance level equals 0.33.

These analyses yielded two main results. First, consistently with the baseline classification results of the TDA classifier and with the results of previous machine learning classifiers, the highest accuracies were obtained in the gamma band for all participants but one [32]. Second, consistently with the hypothesis of dimensionality reduction rearranging the point cloud in shapes that facilitate classification, our results consistently confirm that point clouds in reduced dimensionality spaces yield higher accuracies than the baseline, high-dimensional dataset.

Effect of dimensionality reduction

Since higher classification accuracies are obtained in low dimensional spaces, a question on how accuracy relates to dimension arises. In the case of RFE, we aim to find an optimum number of sources

as guided by previous results [32]. In order to do so, we tested our topological classifier using the spaces resulting of applying recursive feature elimination to the EEG data projected onto the space of sources, increasing the number of selected sources by the algorithm from 2 to 10. Classifications were performed for each participant and each frequency band in parallel.

The case of PCA presents a more involved study of the effect of the dimensionality mainly due to the relationship between accuracy and explained variance. In most machine learning classifiers, there is a direct relationship between the two: the higher the explained variance, the higher the accuracy, often converging once 95% of explained variance is reached. Our hypothesis is that the notion of shape that TDA techniques are able to capture from the data is independent of its variability. Instead, we expect to find an optimum number of principal components such that the resulting projected spaces yield shapes more favourable to be classified. We tested our topological classifier using the spaces resulting from principal component analysis applied to the space of sources, increasing the number of selected principal components at each step from 2 to 10. We recorded the accuracy of each classification as well as the amount of explained variance by the number of components at that step. Classifications were performed for each participant and for each frequency band in parallel. To further assess the effect of independent component analysis to the shape of the data, we also performed the same tests using the space of electrodes, namely the EEG data without applying the ICA algorithm.

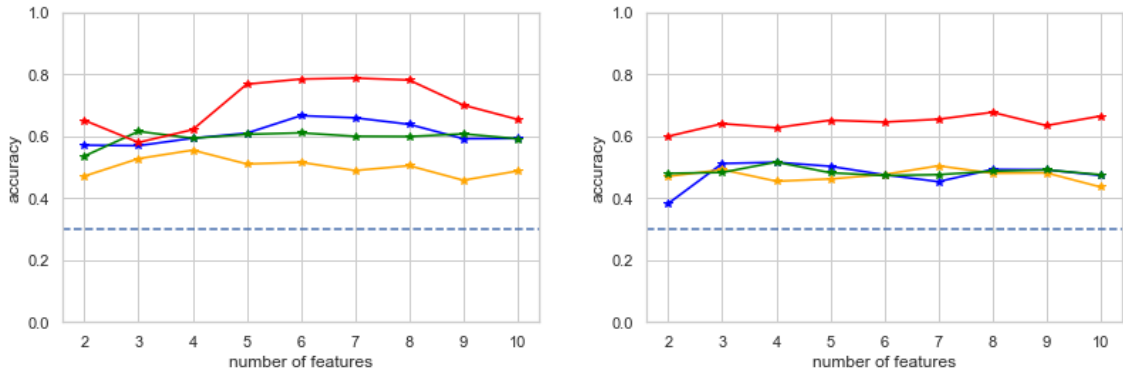


Figure 7: Variation of accuracy of the topological classifier by frequency bands (blue: no filter; yellow: alpha; green: beta; red: gamma) depending on the number of sources selected by recursive feature selection for participants 1 and 2. The blue dotted line indicates chance level.

Figure 7 shows the variation of accuracy of two typical participants with respect to the number of sources selected by RFE (from 2 to 10), separating frequency bands. Higher accuracies are consistently found within the gamma band. The accuracy evolution graph shows that, in general, only a low amount of sources is needed to obtain the best accuracy. More precisely, five sources are enough for the classification task for all participants, which is consistent with the results obtained in [32].

The upper row of Fig. 8 depicts the variation of accuracy with respect to dimension when PCA is applied to the electrode space. A peak is observed in dimensions 3 and 4. By contrast, the lower row in Fig. 8 compares the variation of accuracy with respect to dimension when PCA is applied to the source space. The graphs suggest that the increase of accuracy (red) is essentially independent of the explained variance by PCA (blue), more visibly in the case of electrodes.

3 Discussion

This study has focused on the design and characterization of a novel method of data classification by means of topological data analysis. By contrast to machine learning classifiers, which are based on assessing relative distance metrics across points of different classes, the topological classifier here described is based on exploiting differences in shape between point clouds from each class. Operationally, we quantified such differences by calculating dissimilarities between persistence silhouettes [46].

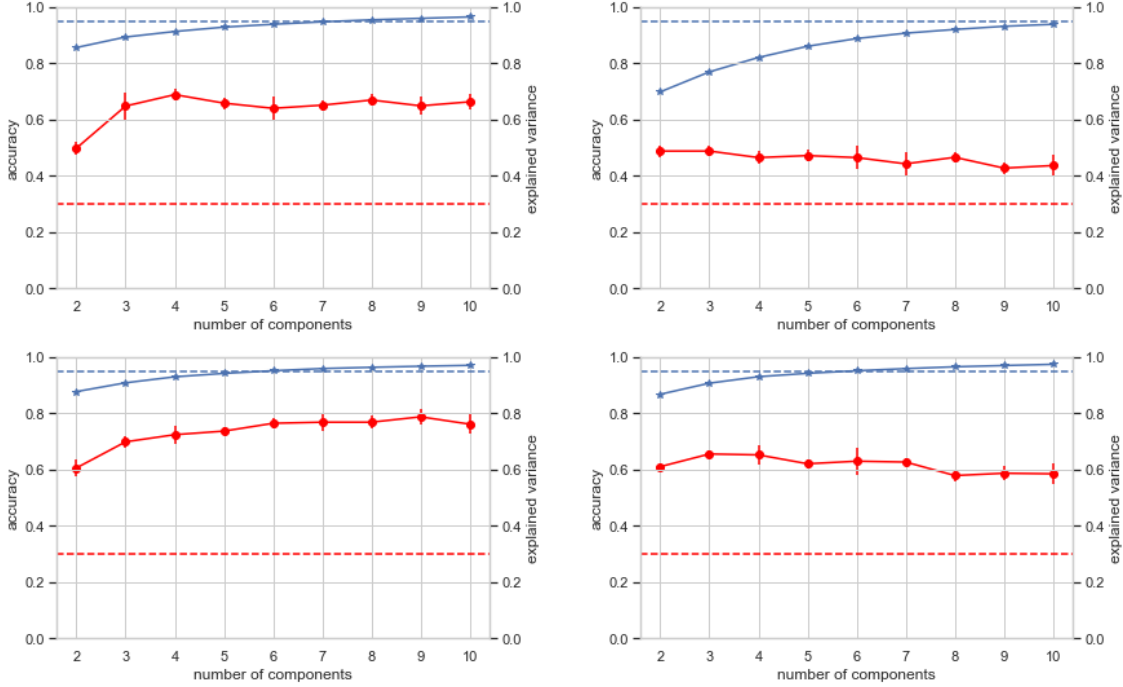


Figure 8: Comparison of variation of accuracy (red) with PCA explained variance (blue) as dimension increases for participants 1 (left) and 2 (right). The upper row corresponds to the space of electrodes and the lower row corresponds to the space of sources. The blue dotted line indicates 95% of explained variance and the red dotted line is chance level. Standard deviations of accuracy (red) are computed after five repetitions of the classifier.

The stability theorem for persistence barcodes [46, 35] guarantees that small variations of a point cloud yield small variations on its persistence descriptors. Because of this, if a point cloud is structured into distinct classes —three in the case of our datasets— addition of a point to the class where it belongs should be barely noticeable on the resulting topological descriptors, while incorporating the same point into the other classes is likely to yield more perceivable shape changes, which we quantify and use for classification purposes. We tested this principle with electro-encephalographic datasets recorded from human participants during a study of motivated behaviour [32], aimed at quantifying the influence of three levels of social pressure on the specifics of neural dynamics of the human motivational system. As for most EEG analyses, the data time series were decomposed into three frequency bands of interest: α , β and γ (see Methods), effectively tripling the analyses, and we also used an unfiltered version of the dataset signals for comparison purposes.

Choice of dataset

The choice of dataset responds to several requirements:

1. The need of having a rich, high-dimensional dataset, which contains data clouds with a significant number of elements.
2. As a means to double validate our tests, it was convenient that the dataset had been previously analyzed by reliable methods, as to offer a clear target of potential accuracies for the TDA classifier. In our case, we had data from eleven participants, having performed 1296 trials each, distributed into three classes.
3. Previous machine learning analyses [32] had yielded consistent best performances for the γ band across participants, with accuracy ranges between 75-90%.

Dimensionality

Our study was carried out first with the space of electrodes and subsequently with a space of brain sources obtained from the space of electrodes by means of independent component analysis (ICA). This technique is convenient from a statistical perspective because the dimensions in the source space are statistically independent from each other, and also from a neuroscience perspective, as it allows a rough estimation of the brain source localization responsible for the data recorded.

We tested the effect of dimensionality by assessing the performance of our TDA classifier with an incremental number of dimensions by means of principal component analysis (PCA), hence gradually increasing explained variance. Our PCA analysis ranged up to ten dimensions to ensure that we covered for over 95% of the data variance. This yielded a remarkable result: while the degree of explained variance increased asymptotically over ten dimensions, the TDA classifier’s accuracy reached a plateau after a certain dimension —often dimension four in the electrode space. This strongly suggests that the classifier’s operation is more sensitive to the latent dimension of the data cloud than to the amount of explained variance. This is reinforced by a comparative analysis with the performance of a 1-NN classifier, which increased its accuracy with increased explained variance up to dimension ten.

As an additional validation analysis of our dimensionality tests, we also performed a recursive feature elimination decomposition (RFE) to identify the signal dimensions in source space contributing the most to the classification. This analysis yielded a similar ceiling effect than PCA, although around dimension five.

Our initial prediction was that a projection of the original dataset onto an independent component space (or source space) via ICA would yield a finer defined cloud and ultimately higher accuracies than those of the original dataset. This hypothesis is supported by our analysis about the influence of dimensionality with the ICA-dataset on the accuracy, which yields a lesser sensitivity when ICA has been previously applied to the dataset. Likewise, our validation test with RFE also shows that there is a minimal number of necessary sources to obtain an asymptotic accuracy (typically five).

Ultimately, the number of dimensions that effectively contribute to the classification with the TDA classifier match the number of sources that suffice to represent the brain network of motivation in the original study [32]. Moreover, the frequency band that yielded the best results is the γ band, consistently with previous results.

Explained variance versus explained shape

The accuracy obtained by our TDA-based classifier is comparable with those of a nearest neighbour classifier (1-NN) and consistent with previous results [32]. However, one of the major differences in performance is the steady increase of accuracy for the 1-NN classifier with the number of dimensions used for classification. In other words, the higher the explained variance of the signals with which the classifier is trained, the better the accuracy. Nonetheless, the accuracies for the TDA classifier typically stall after a certain dimension consistently across subjects. We believe that the higher sensitivity of the 1-NN classifier lays in its local nature, as opposed to the global focus of topological summaries. In conclusion, we could surmise that TDA provides quantitative methods to assess the amount of “explained shape” instead of explained variance by a model. Our results suggest that the effect of the ambient dimension on the shape of a point cloud is of a different nature than its effect on data variance, since shape tends to stabilize at some dimension which is intrinsic to the given data.

Supporting information

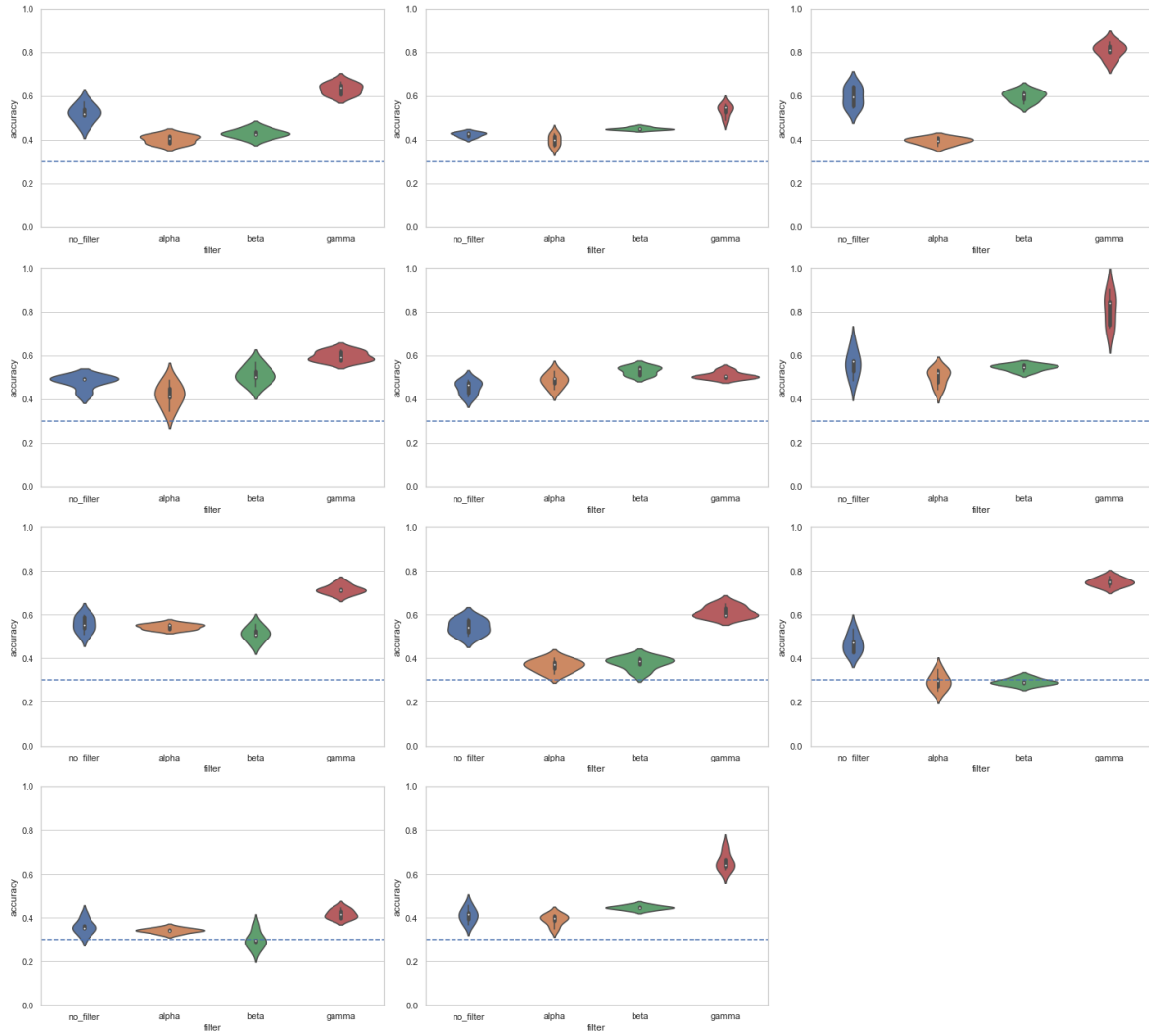


Figure 9: Accuracies of the topological classifier by frequency band (no filter, alpha, beta, and gamma) on the space of sources for participants 1 to 11 without any dimensionality reduction

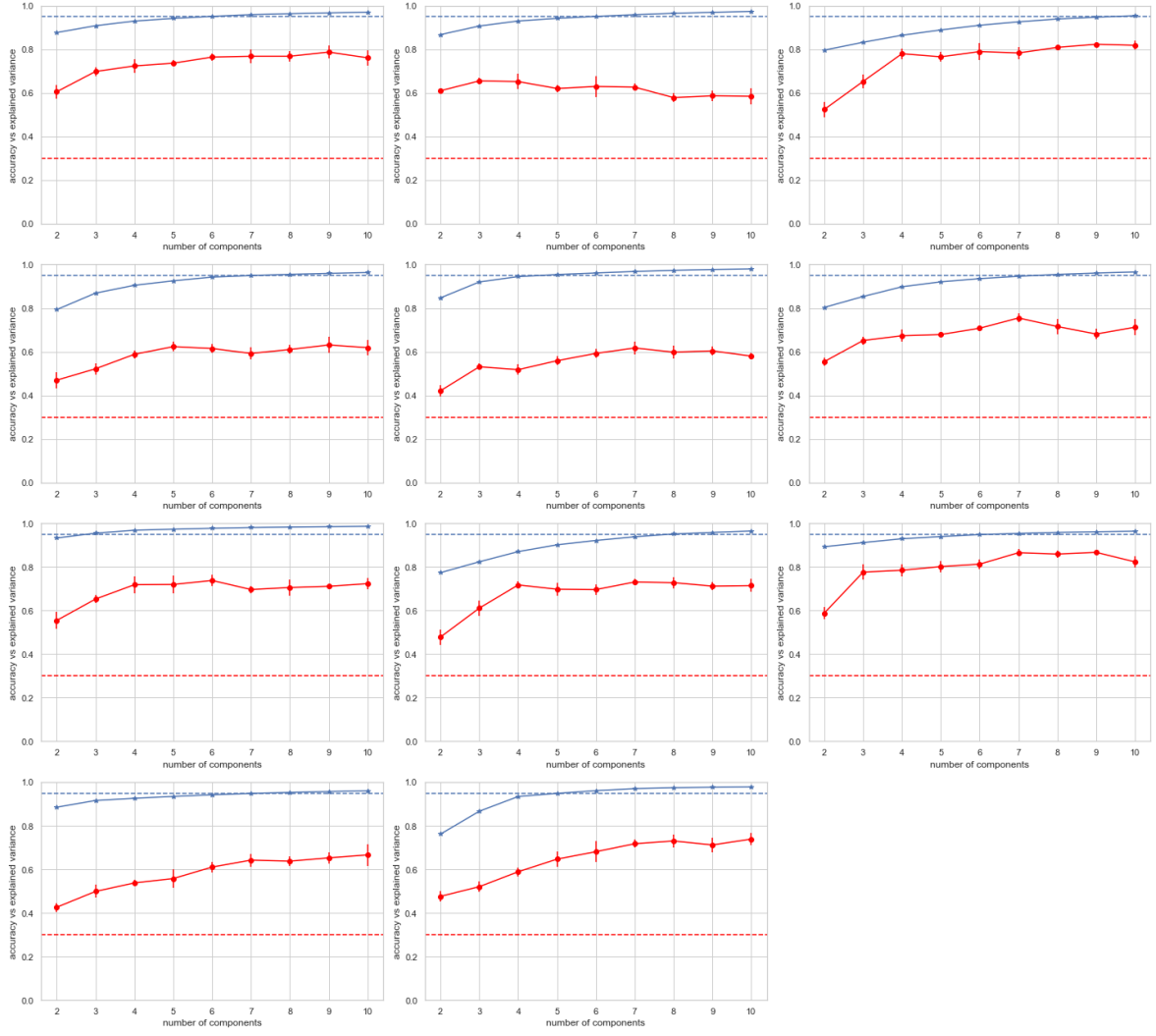


Figure 10: Comparison of variation of accuracy (red) with **PCA** explained variance (blue) as dimension increases for all participants on the **space of sources** within the gamma frequency band. The blue dotted line indicates 95% of explained variance and the red dotted line is chance level. Standard deviations of accuracy (red) are computed after five repetitions of the classifier.

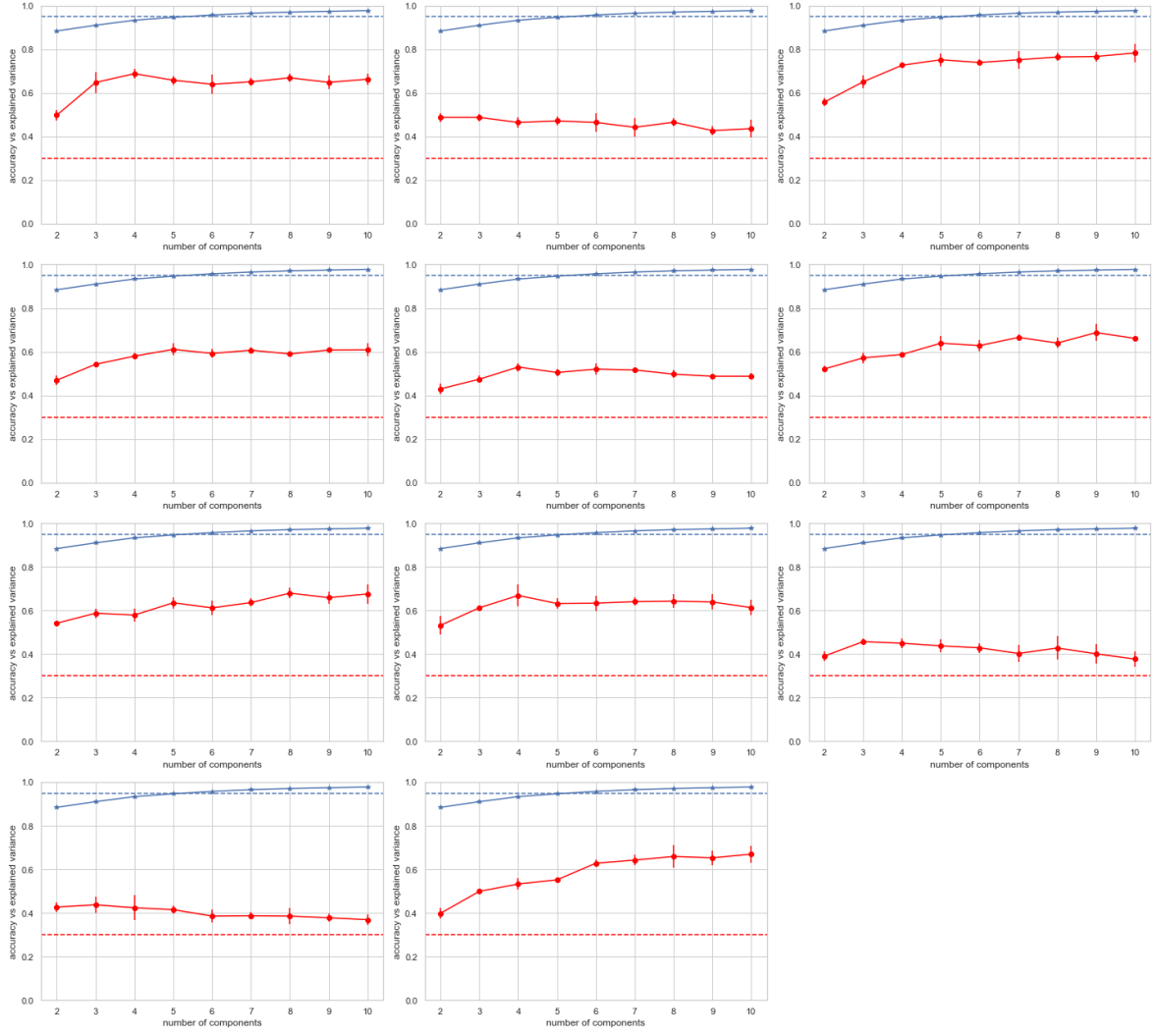


Figure 11: Comparison of variation of accuracy (red) with **PCA** explained variance (blue) as dimension increases for all participants on the **space of electrodes** within the gamma frequency band.

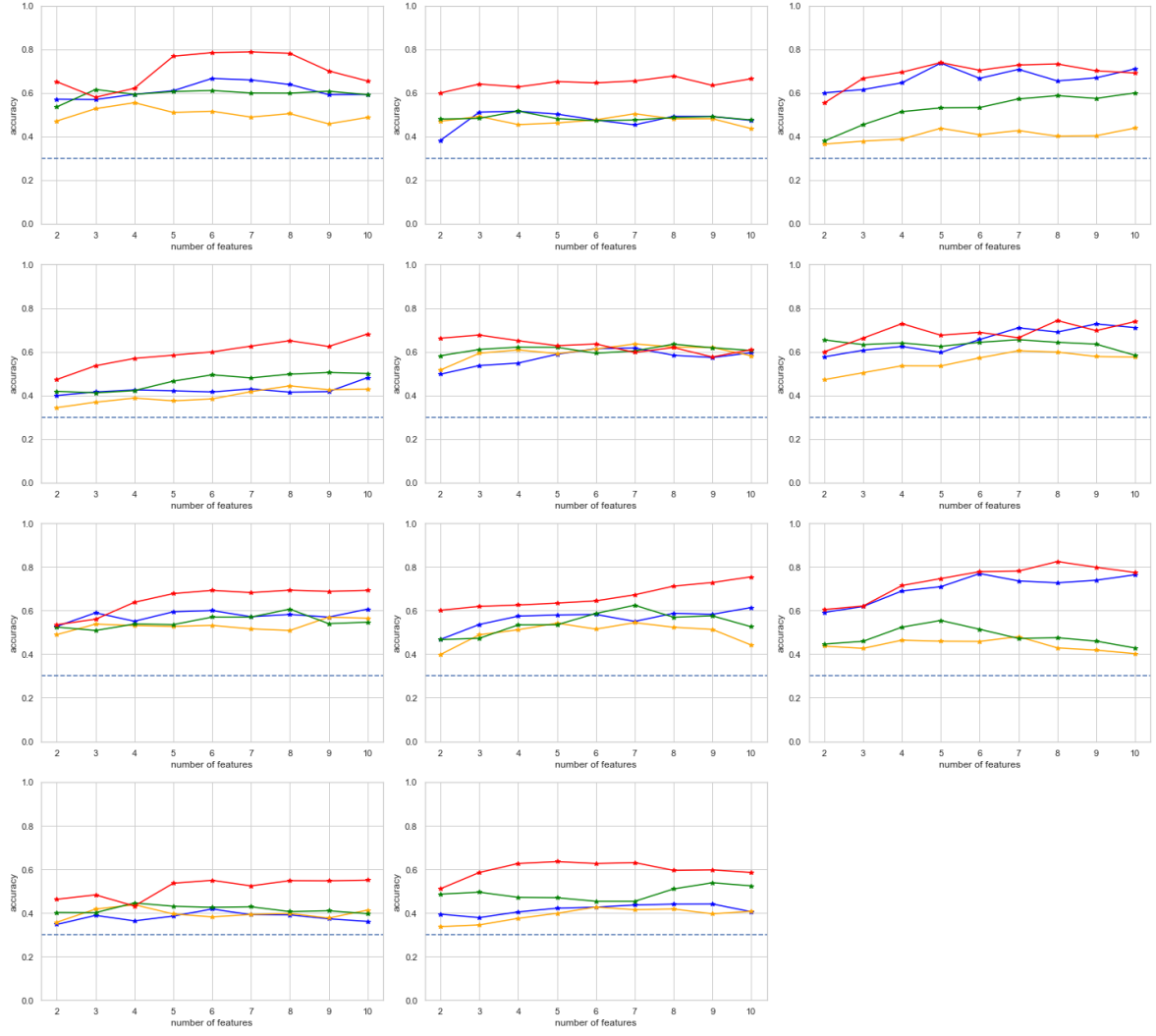


Figure 12: Comparison of variation of accuracy for each frequency band (blue: no filter; yellow: alpha; green: beta; red: gamma) as the number of sources increases from 2 to 10 by the **RFE** algorithm, for all participants on the **space of sources**.

	no filter			alpha			beta			gamma		
	raw	pca	rfe	raw	pca	rfe	raw	pca	rfe	raw	pca	rfe
1	0.57	0.56	0.69	0.42	0.60	0.58	0.46	0.64	0.65	0.67	0.79	0.83
2	0.43	0.47	0.54	0.41	0.52	0.58	0.46	0.56	0.54	0.56	0.66	0.71
3	0.65	0.56	0.77	0.49	0.48	0.50	0.63	0.63	0.65	0.85	0.82	0.76
4	0.50	0.48	0.50	0.41	0.52	0.48	0.57	0.56	0.53	0.62	0.63	0.70
5	0.49	0.58	0.65	0.53	0.67	0.68	0.55	0.66	0.68	0.54	0.62	0.70
6	0.65	0.63	0.77	0.53	0.64	0.66	0.56	0.74	0.70	0.90	0.75	0.78
7	0.60	0.57	0.65	0.56	0.54	0.59	0.56	0.55	0.63	0.75	0.74	0.75
8	0.58	0.54	0.66	0.40	0.53	0.59	0.40	0.67	0.64	0.65	0.73	0.79
9	0.51	0.64	0.79	0.35	0.47	0.53	0.32	0.49	0.60	0.78	0.87	0.85
10	0.41	0.42	0.44	0.36	0.51	0.49	0.36	0.51	0.48	0.45	0.67	0.59
11	0.46	0.43	0.50	0.41	0.42	0.47	0.46	0.53	0.59	0.72	0.74	0.66

Figure 13: Comparison of baseline accuracies (*raw*) of the topological classifier on source space for each frequency band with accuracies obtained after dimensionality reduction with principal component analysis (*pca*) and recursive feature elimination (*rfe*), for participants 1 to 11. The highest accuracies are marked in boldface.

no filter			alpha		
raw	pca	rfe	raw	pca	rfe
0.57 \pm 0.04	0.56 \pm 0.06	0.69 \pm 0.04	0.42 \pm 0.02	0.60 \pm 0.01	0.58 \pm 0.04
0.43 \pm 0.01	0.47 \pm 0.02	0.54 \pm 0.05	0.43 \pm 0.03	0.52 \pm 0.03	0.58 \pm 0.04
0.65 \pm 0.05	0.56 \pm 0.03	0.77 \pm 0.06	0.41 \pm 0.02	0.48 \pm 0.02	0.50 \pm 0.04
0.50 \pm 0.03	0.48 \pm 0.04	0.50 \pm 0.03	0.49 \pm 0.05	0.52 \pm 0.02	0.48 \pm 0.04
0.49 \pm 0.03	0.56 \pm 0.03	0.65 \pm 0.04	0.53 \pm 0.03	0.67 \pm 0.03	0.68 \pm 0.04
0.65 \pm 0.06	0.63 \pm 0.05	0.77 \pm 0.06	0.53 \pm 0.04	0.64 \pm 0.02	0.66 \pm 0.05
0.60 \pm 0.04	0.57 \pm 0.06	0.65 \pm 0.04	0.56 \pm 0.01	0.54 \pm 0.02	0.59 \pm 0.03
0.58 \pm 0.03	0.54 \pm 0.03	0.66 \pm 0.05	0.40 \pm 0.03	0.53 \pm 0.02	0.59 \pm 0.06
0.54 \pm 0.05	0.64 \pm 0.04	0.79 \pm 0.06	0.35 \pm 0.04	0.47 \pm 0.03	0.53 \pm 0.03
0.41 \pm 0.03	0.42 \pm 0.06	0.44 \pm 0.03	0.36 \pm 0.01	0.51 \pm 0.03	0.49 \pm 0.03
0.46 \pm 0.03	0.43 \pm 0.01	0.50 \pm 0.04	0.41 \pm 0.03	0.42 \pm 0.02	0.47 \pm 0.04

Table 1: Comparison of baseline accuracies (*raw*) of the topological classifier on source space for each frequency filter with accuracies obtained after dimensionality reduction with principal component analysis (*pca*) and recursive feature elimination (*rfe*), with no frequency filter and in the alpha frequency band, for patients 1 to 11 with standard deviations after five repetitions.

beta			gamma		
raw	pca	rfe	raw	pca	rfe
0.46 ± 0.02	0.64 ± 0.03	0.65 ± 0.03	0.67 ± 0.03	0.79 ± 0.03	0.83 ± 0.08
0.46 ± 0.01	0.56 ± 0.03	0.54 ± 0.03	0.56 ± 0.03	0.66 ± 0.01	0.71 ± 0.04
0.63 ± 0.03	0.63 ± 0.02	0.65 ± 0.07	0.85 ± 0.03	0.82 ± 0.01	0.76 ± 0.06
0.57 ± 0.04	0.56 ± 0.02	0.53 ± 0.04	0.62 ± 0.02	0.63 ± 0.04	0.70 ± 0.07
0.55 ± 0.02	0.66 ± 0.04	0.68 ± 0.02	0.54 ± 0.02	0.62 ± 0.03	0.70 ± 0.04
0.56 ± 0.01	0.74 ± 0.02	0.70 ± 0.03	0.90 ± 0.08	0.75 ± 0.02	0.78 ± 0.05
0.56 ± 0.03	0.55 ± 0.01	0.63 ± 0.04	0.75 ± 0.02	0.74 ± 0.02	0.75 ± 0.06
0.40 ± 0.03	0.67 ± 0.02	0.64 ± 0.05	0.65 ± 0.03	0.73 ± 0.02	0.79 ± 0.06
0.32 ± 0.01	0.49 ± 0.03	0.60 ± 0.05	0.78 ± 0.02	0.87 ± 0.01	0.85 ± 0.08
0.36 ± 0.04	0.51 ± 0.03	0.48 ± 0.03	0.45 ± 0.02	0.67 ± 0.05	0.59 ± 0.05
0.46 ± 0.01	0.53 ± 0.02	0.59 ± 0.04	0.72 ± 0.04	0.74 ± 0.03	0.66 ± 0.04

Table 2: Comparison of baseline accuracies (*raw*) of the topological classifier on source space for each frequency filter with accuracies obtained after dimensionality reduction with principal component analysis (*pca*) and recursive feature elimination (*rfe*), in the beta and gamma frequency bands, for patients 1 to 11 with standard deviations after five repetitions.

References

- [1] Grossberg S. A path toward explainable AI and autonomous adaptive intelligence: Deep learning, adaptive resonance, and models of perception, emotion, and action. *Front Neurobot* 2020; 14.
- [2] Sumathi A, Yasotha K, Nandhinidevi S. High dimensional deep data clustering architecture towards evolving concept. *NVEO - Natural Volatiles & Essential Oils Journal* 2021; 1695–1703.
- [3] Yazdani A, Lu L, Raissi M, Karniadakis GE. Systems biology informed deep learning for inferring parameters and hidden dynamics. *PLOS Computational Biology* 2020; 16:e1007575.
- [4] Moen E, Bannon D, Kudo T, Graf W, Covert M, Van Valen D. Deep learning for cellular image analysis. *Nat Methods* 2019; 16:1233–1246.
- [5] Wang L, Wang H, Huang Y, Yan B, Chang Z, Liu Z, Zhao M, Cui L, Song J, Li F. Trends in the application of deep learning networks in medical image analysis: Evolution between 2012 and 2020. *European Journal of Radiology* 2022; 146:110069.
- [6] Pathak AR, Pandey M, Rautaray S. Application of Deep Learning for Object Detection. *Procedia Computer Science* 132: 1706–1717, 2018.
- [7] Gibson PB, Chapman WE, Altinok A, Delle Monache L, DeFlorio MJ, Waliser DE. Training machine learning models on climate model output yields skillful interpretable seasonal precipitation forecasts. *Commun Earth Environ* 2021; 2:1–13.
- [8] Rasp S, Pritchard MS, Gentine P. Deep learning to represent subgrid processes in climate models. *PNAS* 2018; 115:9684–9689.
- [9] Zou J, Huss M, Abid A, Mohammadi P, Torkamani A, Telenti A. A primer on deep learning in genomics. *Nat Genet* 2019; 51:12–18.
- [10] Ghassemi M, Oakden-Rayner L, Beam AL. The false hope of current approaches to explainable artificial intelligence in health care. *The Lancet Digital Health* 2021; 3:e745–e750.
- [11] Petch J, Di S, Nelson W. Opening the black box: The promise and limitations of explainable machine learning in cardiology. *Canadian Journal of Cardiology* 2021.

- [12] Razavi S. Deep learning, explained: Fundamentals, explainability, and bridgeability to process-based modelling. *Environmental Modelling & Software* 2021; 144:105159.
- [13] Heaven D. Why deep-learning AIs are so easy to fool *Nature* 2019; 574:163–166.
- [14] LeCun Y, Bengio Y, Hinton G. Deep learning. *Nature* 2015 May; 521:436–444.
- [15] Nguyen A, Yosinski J, Clune J. Deep neural networks are easily fooled: High confidence predictions for unrecognizable images. 2015 IEEE Conference on Computer Vision and Pattern Recognition (CVPR), 2015; 427–436.
- [16] Belchi F, Pirashvili M, Conway J, Bennett M, Djukanovic R, Brodzki, J. Lung topology characteristics in patients with chronic obstructive pulmonary disease. *Scientific Reports* 2018; 8(1):1–12.
- [17] Sizemore AE, Phillips-Cremins JE, Ghrist R, Baset DS. The importance of the whole: Topological data analysis for the network neuroscientist. *Network Neuroscience* 2018; 3(3):656–673.
- [18] Lawson P, Sholl AB, Brown, JQ, Fasy BT, Wenk C. Persistent homology for the quantitative evaluation of architectural features in prostate cancer histology. *Scientific Reports* 2019; 9(1):1–15.
- [19] Xia K, Zhao Z, Wei G-W. Multiresolution persistent homology for excessively large biomolecular datasets. *The Journal of Chemical Physics* 2015; 143(13): 10B603.1.
- [20] Hiraoka Y, Nakamura T, Hirata A, Escolar EG, Matsue K, Nishiura Y. Hierarchical structures of amorphous solids characterized by persistent homology. *Proceedings of the National Academy of Sciences* 2016; 113(26):7035–7040.
- [21] Gebhart T, Schrater P. Adversary detection in neural networks via persistent homology. *arXiv:1711.10056*, 2017.
- [22] Pearson K. LIII. On lines and planes of closest fit to systems of points in space. *The London, Edinburgh, and Dublin Philosophical Magazine and Journal of Science* 1901; 2(11):559–572.
- [23] Comon, P. Independent Component Analysis. *Higher-Order Statistics* 1992; 29–38.
- [24] Carrière M, Blumberg A. Multiparameter persistence images for topological machine learning. *Conference on Neural Information Processing Systems*, 2020.
- [25] Hofer C, Kwitt R, Niethammer M, Uhl A. Deep learning with topological signatures. *arXiv:1707.04041*, 2017.
- [26] Yan Y, Ivanov K, Cen J, Liu Q-H, Wang, L. Persistence landscape based topological data analysis for personalized arrhythmia classification. *Preprints* 2019, 2019080320.
- [27] Kindelan R, Frías J, Cerda M, Hitschfeld N. Classification based on topological data analysis. *arXiv:2102.03709*, 2021.
- [28] Inés A, Domínguez C, Heras J, Mata G, Rubio J. Semi-supervised machine learning: A homological approach. *arXiv:2301.11658*, 2023.
- [29] Allen EA, Damaraju E, Eichele T, Wu L, Calhoun VD. EEG Signatures of Dynamic Functional Network Connectivity States. *Brain Topogr.* 2017; 1–16.
- [30] Cattai T, Colonnese S, Corsi M-C, Bassett DS, Scarano G, De Vico Fallani F. Characterization of mental states through node connectivity between brain signals. 26th European Signal Processing Conference (EUSIPCO): 1377–1381.
- [31] Gilson M, Zamora-López G, Pallarés V, Adhikari MH, Senden M, Campo AT, Mantini D, Corbetta M, Deco G, Insabato A. Model-based whole-brain effective connectivity to study distributed cognition in health and disease. *Network Neuroscience* 2019; 4:338–373.

- [32] Cos I, Deco G, Gilson M. Behavioural and neural correlates of social pressure during decision-making of precision reaches. DOI:10.21203/rs.3.rs-1974463/v1
- [33] Edelsbrunner H, Letscher D, Zomorodian A. Topological persistence and simplification. *Discrete & Computational Geometry* 2002; 28:511–533.
- [34] Zomorodian A, Carlsson G. Computing persistent homology. *Discrete & Computational Geometry* 2005; 33(2):249–274.
- [35] Edelsbrunner H, Harer J. Persistent homology – a survey. *Surveys on Discrete and Computational Geometry: Twenty Years Later. Contemporary Mathematics* 2008; 453:257–282; Providence: American Mathematical Society.
- [36] Carlsson G. Topology and data. *Bulletin of the American Mathematical Society (N.S.)* 2009; 46(2):255–308.
- [37] De Silva V, Ghrist R. Coverage in sensor networks via persistent homology. *Algebraic & Geometric Topology* 2007; 7(1): 339–358.
- [38] Ghrist R. Barcodes: the persistent topology of data. *Bulletin of the American Mathematical Society* 2008; 45(1):61–75.
- [39] Hatcher A. *Algebraic Topology*. Cambridge: Cambridge University Press, 2002.
- [40] The GUDHI Project. GUDHI User and Reference Manual, ed. 3.4.1. GUDHI Editorial Board, 2021.
- [41] Cohen-Steiner D, Edelsbrunner H, Harer J. Stability of persistence diagrams. *Discrete & Computational Geometry* 2007; 37(1):103–120.
- [42] Chazal F, De Silva V, Oudot S. Persistence stability for geometric complexes. *Geometriae Dedicata* 2014; 173:193–214.
- [43] Mileyko Y, Mukherjee S, Harer J. Probability measures on the space of persistence diagrams. *Inverse Problems* 2011 Nov; 27(12):124007.
- [44] Bubenik, P. Statistical topological data analysis using persistence landscapes *J. Mach. Learn. Res.* 2015; 16(1): 77–102.
- [45] Bubenik P, Dłotko P. A persistence landscapes toolbox for topological statistics. *Journal of Symbolic Computation* 2017; 78:91–114.
- [46] Chazal F, Fasy BT, Lecci F, Rinaldo A, Wasserman L. Stochastic convergence of persistence landscapes and silhouettes. *Proceedings of the Thirtieth Annual Symposium on Computational Geometry*, 2014:474–483.
- [47] Virtanen P et al. SciPy 1.0: Fundamental Algorithms for Scientific Computing in Python. *Nature Methods* 2020; 17:261–272.
- [48] Pedregosa F et al. Scikit-learn: Machine Learning in Python. *Journal of Machine Learning Research* 2011; 12:2825–2830.
- [49] Guyon I, Weston J, Barnhill S, Vapnik V. Gene selection for cancer classification using support vector machines. *Machine Learning* 2002; 46(1-3):389–422.
- [50] Waskom ML. Seaborn: Statistical data visualization. *Journal of Open Source Software* 2021; 6(60):3021.